Long-term permeability evolution of shale seal rocks with argon and scCO$_2$

Arash Kamali-Asl [a], Anthony R. Kovscek, Ph.D. [a,*], Mark D. Zoback [b]

[a] *Department of Energy Resources Engineering, Stanford University, Stanford, USA*
[b] *Department of Geophysics, Stanford University, Stanford, USA*

A R T I C L E   I N F O

A B S T R A C T

We conducted a suite of experiments to evaluate the long-term permeability evolution of shale rocks under constant effective stress, before, during, and after interaction with supercritical carbon dioxide (scCO$_2$). To do so, we measured the time-dependent evolution of argon permeabilities for the pre- and post-reacted samples (i.e., before and after long-term interaction with scCO$_2$). In addition, we obtained permeability evolution during long-term interaction with scCO$_2$. The samples showed either relatively constant permeabilities or a moderate decrease during pre-reaction long-term argon tests. The permeability evolution during long-term CO$_2$ tests showed continuous increase, continuous decrease, or cycles of increase/decrease in permeability. The long-term response of the samples to CO$_2$ included phenomena such as (i) salt precipitation, (ii) swelling-induced cracks, and (iii) carbonate dissolution. While it is obvious that salt precipitation and swelling-induced cracks decrease and increase the permeability, respectively, the sample response to carbonate dissolution proved to be more complex and may increase or decrease the permeability. The permeability evolution during post-reaction long-term argon injection is also affected by the contribution of each of these three phenomena, during long-term interaction with CO$_2$. We observe increase, decrease, and constant permeability evolution during post-reaction argon tests. Our experiments reveal that the initial permeability of the samples plays a significant role on the long-term permeability response of shales in the presence argon and scCO$_2$ fluids. This study shows that when shales are hydraulically fractured with CO$_2$ their initial permeability has a more significant role than their permeability evolution over time.

1. Introduction

Carbon dioxide could replace water as the hydraulic fracturing fluid in shale reservoirs (Gandossi and Von Estorff, 2013; Middleton et al., 2015). CO$_2$-fracturing has not yet been implemented as an industry practice, but it has the potential to address: (i) the scarcity of water in dry regions where most shale reservoirs are located and (ii) more economic approaches of storing CO$_2$ underground (Song et al., 2019). Employing CO$_2$ as the hydraulic fracturing fluid entails technical differences as compared to water. The lower viscosity of CO$_2$ compared to water could increase or decrease the efficiency of a stimulation program. Its lower viscosity is associated with smaller shear force in the network of shear fractures; hence the production efficiency of shear hydraulic fractures might be negatively affected. However, it can provide better access to the rock mass that is not adjacent to hydraulic fractures, by reducing diffusion time, and subsequently, greater production rates can be achieved (Hakso and Zoback, 2019).

Shales typically have a very complex micro-structure and ultra-low permeabilities, with a wide range of mineralogical content and organic matter (Heller et al., 2014; Zoback and Kohli, 2019). A successful CO$_2$-fracturing stimulation program requires a thorough understanding of the interactions between injected CO$_2$, reservoir rock, and in-situ water (Lindner, 2016; Fatah et al., 2020). Mineral dissolution/precipitation (mainly in carbonate minerals), CO$_2$ adsorption into clays and kerogen, and salt/mineral precipitation are among the most influential phenomena altering the permeability of shale rocks as they interact with supercritical carbon dioxide (scCO$_2$). Carbonate dissolution might increase or decrease permeability (Lindner, 2017). Adsorption and salt/mineral precipitation, on the other hand, decrease the permeability of shale rocks (Lyu et al., 2018). Adsorption, in turn, results in swelling strain in clays and organic matter (Ao et al., 2017; Lindner, 2017; Lyu et al., 2018; Zou et al., 2018), leading to development of swelling-induced micro-cracks (Meng et al., 2020; Wei et al., 2019). Due to the complex micro-structure of shale rocks, their response to interaction with scCO$_2$ is often sample-dependent and can be attributed to their mineralogical content, initial permeability,

---

* Corresponding author.
E-mail addresses: akamalia@stanford.edu (A. Kamali-Asl), kovscek@stanford.edu (A.R. Kovscek).

micro-structure, tortuosity, initial water saturation, and so on (Al Shafloot et al., 2021). Some research groups have studied the interactions between dry CO_2 or brine-saturated CO_2 and shale rocks by only examining the alterations to their micro-structure (Lu et al., 2016; Sanguinito et al., 2018; Hadian and Rezaee, 2020; Kutchko et al., 2020). Some have focused on influence of rock-CO_2 interaction on changes in permeability and porosity of shale rocks (Al Ismail et al., 2014; Wu et al., 2017; Zhang and Ranjith, 2018; van Noort and Yarushina, 2019; Kamali-Asl et al., 2021).

When (in-situ) water and CO_2 react, carbonic acid (H_2CO_3) is formed which subsequently reacts with the carbonate minerals resulting in their dissolution (Lindner, 2016; Lindner, 2017; Elkady and Kovscek, 2020; Foroutan et al., 2021). Therefore, the micro-structure of the rock may be impacted by creation of new pores and/or altering the surface of calcite/dolomite-filled fractures. This, in turn, may lead to changes in transport and mechanical characteristics of shale reservoirs. Carbonate dissolution might alter the permeability of shale rocks in three ways. The short-term effect is an increase in permeability by increasing pore/fracture-scale porosity (Kamali-Asl et al., 2021). Over longer time periods, however, carbonate dissolution might lead to weakening of the rock matrix (due to dissolution of stiff carbonate minerals), and therefore, closure of some pore throats under constant effective stress, resulting in a decrease of permeability (Teklu et al., 2017).

Precipitation of already-dissolved minerals along the flow path is another process that might occur over longer time periods, causing a decrease in permeability (Liu et al., 2012). Adsorption of CO_2 into the clay minerals and organic matter, due to preferred adsorption of CO_2 over methane, is another phenomenon that occurs when shale rocks interact with CO_2 (Heller and Zoback, 2014). When CO_2 is injected/interacted into/with shale rocks, the formation water evaporates, that in turn, leads to an increase in concentration of dissolved salts in pore water. As the salt concentration reaches the solubility limit, we expect that salt crystals precipitate along the flow path (Nooraiepour et al., 2018). Both phenomena reduce the permeability of shales, although, adsorption is mostly recoverable while salt precipitation is not.

Shales exhibit viscoplastic (creep) deformation under constant stress, which is a time-dependent phenomenon. Clay minerals and organic matter, micro-cracks, and pores with different sizes are among the primary sources of creep deformation in shales (Zoback and Kohli, 2019). The mechanical aspects of creep deformation, i.e., Young's modulus and axial/radial strains, have been thoroughly studied by other researchers (Sone and Zoback, 2013; Kamali-Asl et al., 2018; Rassouli and Zoback, 2018). There is only one paper, however, that discusses implications of creep (time-dependent) deformation on transport properties of shale rocks (Chhatre et al., 2014). They have reported the oil permeability of Vaca Muerta Shale samples at 4 levels of confining stress, with each level lasting for 1–4 weeks depending on the confining level. They found that at lesser confining pressures, the rate of permeability reduction over time is more significant.

Despite the significance of the work by Chhatre et al. (2014), their study is not relevant to the cases where shale rocks interact with carbon dioxide in the context of CO_2 fracturing. To the best of our knowledge, there are no papers in the literature on the effects of $scCO_2$ on time-dependent permeability evolution of shale rocks, under constant stress conditions. In this study, we experimentally investigate the long-term permeability evolution of Wolfcamp Shale samples under constant stress with argon gas before and after long-term interaction with $scCO_2$. Moreover, the $scCO_2$ permeability values are also measured while the rock sample and $scCO_2$ interact. Due to the nature of the shale rocks, they usually have very low permeabilities, and thus, we use the modified pulse decay method (Brace et al., 1968) to estimate their permeability. Note that the experiments reported here each took 3–6 months to complete, and therefore, we believe the long-term results are helpful for modelling studies concerning CO_2-fracturing or caprock seal integrity of CCS projects.

2. Materials and methods

2.1. Samples

The samples were retrieved from a well in Reagan County, TX located in the Midland basin, drilled through a horizontal well in the Wolfcamp formation, as part of the Hydraulic Fracturing Test Site I (HFTS-I) project. We obtained the mineralogical content of the cores using a Rigaku MiniFlex 600 XRD machine, as shown in Table 1. In order to prepare the cores to conduct the permeability experiments, we subcored them into 1-inch diameter cylindrical plugs with lengths of 0.2–0.3 inches. We did not dry the samples to allow for interaction of carbonates with $scCO_2$ in the presence of (in-situ) pore water. Please note that the samples used in this study are obtained from the same sample set as those used in our previous paper on shorter-term effects of $scCO_2$ on permeability of unconventional reservoirs (Kamali-Asl et al., 2021).

2.2. Experimental procedure

We performed the permeability experiments using a hydrostatic test chamber, thermally isolated by polystyrene insulation. The temperature inside the test chamber was maintained using heaters, a fan, and a thermostat. We monitored the temperature at different locations inside the test chamber throughout the experiments using an Omega temperature probe. Each sample was placed between two core-holders using a thick Viton jacket and wired by flexible steel wires to make sure the mineral oil (which is used to apply confining pressure using a Teledyne ISCO pump) does not contact the sample. Upstream and downstream pore pressures were applied, through a Quizix 6000 pump, using pore pressure tubes that were connected to the core-holders with argon and $scCO_2$ as the pore fluids.

2.3. Experimental program

Fig. 1 shows a descriptive generic stress path for the tests. A confining pressure of ~1 MPa is first applied for 24 h, followed by vacuuming the sample for 24 h. The confining pressure is then increased to 20 MPa and a pore pressure of 10 MPa, using argon gas, is applied to both upstream and downstream sides. We let the sample equilibrate for 24–72 h, depending on the initial permeability of the sample. After the initial vacuuming/equilibration of the sample, we start the permeability measurements. In general, the permeability of each sample is measured every 2–4 days, under constant simple effective stress of $\sigma' = P_C - P_P = 40 - 10 = 30$ MPa. This stage of the experiment takes ~3–4 weeks and is conducted to investigate the permeability evolution of the sample under interaction with a non-reactive fluid (i.e., argon). In the absence of chemical reactions between pore fluid and the rock matrix, due to inert nature of argon gas, the permeability evolution is likely to be caused by mechanical processes such as viscoplastic mechanical creep, stress corrosion (Atkinson, 1979), and pressure (dis)solution.

We then remove the argon gas, vacuum the sample and pore pressure tubes for 24 h, introduce $scCO_2$ as the pore fluid, and let it equilibrate with the sample for ~72 h. Afterwards, we measure $scCO_2$ permeability every 2–4 days, for a period of 3–9 weeks, under the same (simple) effective stress of 30 MPa as the argon stage. This second stage of the test

Table 1
Details of samples from HFTS-I using semiquantitative XRD. Percentages are by weight.

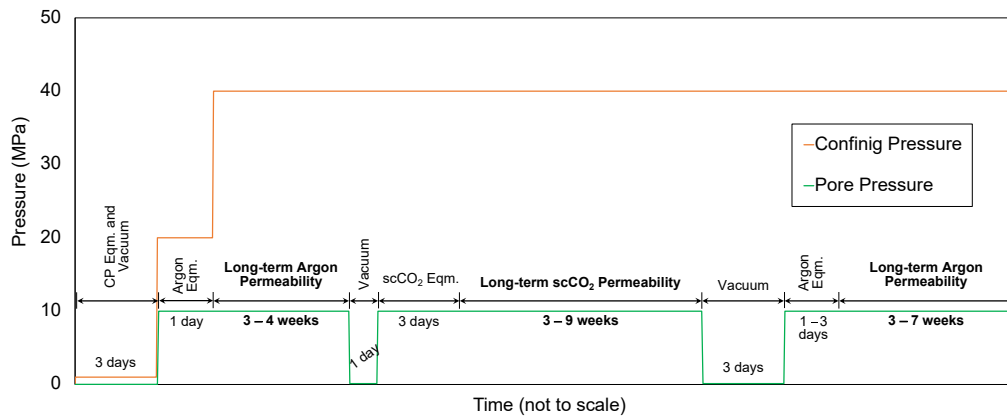| Sample ID	Depth (ft)	QFP (%)	Carbonates (%)	Clays (%)	TOC (%)
1-1H	9285	65	12	19	4
6-1H	11,588	56	21	20	3
6-3H	11,662	25	67	7	1
6-4H	11,673	52	7	35	6

Fig. 1. Typical stress path followed during the experiments.

is, however, accompanied by chemical interactions between the pore fluid (i.e., scCO$_2$), the rock matrix, and the in-situ residual water in the sample. Mineral dissolution, in particular, is expected to occur by interaction between carbonates (i.e., often calcite and seldom dolomite) and carbonic acid (that is formed by interaction of in-situ water and scCO$_2$). Therefore, the permeability evolution during this stage is affected by both time-dependent chemical and mechanical processes.

Lastly, CO$_2$ is removed from the sample, and it is vacuumed for 72 h to remove any residual CO$_2$ from the sample and pore pressure tubes. Then, argon is reintroduced and equilibrated with the sample (for 24–72 h) and its permeability is measured every 2–4 days, for a period of 3–7 weeks, depending on the sample. Identical with stages 1 and 2, the (simple) effective stress is held constant throughout the stage at 30 MPa. This stage is conducted to investigate how long-term interaction with scCO$_2$ (i.e., stage 2) might affect the time-dependent evolution of permeability with an inert gas (i.e., argon) as the pore fluid. In this way, the pre- and post-scCO$_2$ measurements with argon serve as control tests. Please note that the temperature in the chamber was set at ~40 °C to make sure that CO$_2$ is supercritical.

2.4. Permeability measurement

The test media (chamber and sample) before, during, and after interaction with scCO$_2$ were all the same. The permeability was measured using the modified pulse-decay method (Brace et al., 1968). In this method, we first set upstream and downstream pore pressures at 10 MPa. Then, the upstream pore pressure is increased by 0.3–1.5 MPa (depending on the sample) to induce pressure diffusion, while practically no fluid flow occurs over the experimental time-scales due to very low permeability values. The upstream pore pressure is then maintained at a constant value (at 10.3–11.5 MPa; depending on the sample) that eliminates the experimental errors associated with leakage at the upstream side. On the other hand, the downstream pore pressure is left uncontrolled (at an initial value of 10 MPa) and its evolution is recorded, which increases over time to reach to upstream pore pressure. The time-dependent differential pore pressure, ΔP(t), follows an exponential evolution expressed as (Brace et al., 1968)

$$\Delta P(t) = \Delta P_0 e^{-\alpha t} \tag{1}$$

where ΔP(t) and ΔP$_0$ are differential pore pressures at time t and 0, respectively, and α is the slope of the plot of log (ΔP(t)) vs. time. Then, permeability is estimated as (Brace et al., 1968)

$$k = \frac{\alpha \beta V_{down} L \mu}{A} \tag{2}$$

where β is isothermal gas compressibility (Pa^{-1}) at a given pressure and temperature and V$_{down}$ is the downstream volume (m^3). Please note that

it is assumed that no fluid flow occurs from upstream to downstream, therefore, the downstream volume should be constant throughout the experiment, otherwise, the measurements violate the assumptions.

2.5. Imaging

A Thermo Fisher Scientific Apreo S LoVac Scanning Electron Microscope (SEM) was used to conduct pore-scale imaging. The imaging was performed in Back-Scattered Electron (BSE) mode, in which, the brightness/darkness of the different regions are proportional to elemental mass thereby indicating different minerals, organic matter, or porosity. Energy Dispersive Spectroscopy (EDS) maps were also obtained in order to identify micro-structural changes of the elemental composition.

3. Results and data analysis

In this section, we present the data for each sample. Because the study samples derive from a large field-scale project (Ciezobka et al., 2018), the presentation of the experimental results is categorized based on the sample number to be consistent with other studies in this large-scale project (e.g., Kamali-Asl et al., 2021). Discussion is provided in section 4.

3.1. Sample 6-1H

Fig. 2 shows the evolution of permeability for sample 6-1H, over a period of 12 weeks, in which the experiment is divided into 8 stages. Note that the pore pressures were kept constant at 10 MPa, throughout the experiment. In Stage 1, we measure argon permeability at consecutive (simple) effective stresses (σ' = CP–PP) of [10, 30, 10] MPa. We then let the sample interact with scCO$_2$ for 3 days, followed by the same permeability cycle as argon, denoted as Stage 2. Taking the permeability values at σ' = 30 MPa, we observe an increase in permeability by 163% when transitioning from an argon (i.e., Stage 1) to a CO$_2$ cycle (i.e., Stage 2). As we have discussed in our previous paper (Kamali-Asl et al., 2021), an increase in permeability after interaction with scCO$_2$ is potentially attributed to carbonate dissolution. Subsequently, we conducted Stage 3 by re-introducing argon and measuring permeability at σ' = [10, 30] MPa. What we observe is that argon permeability in Stage 3 (i.e., after interaction with scCO$_2$) is smaller than Stage 1 (i.e., before interaction with scCO$_2$), despite greater CO$_2$ permeability and potential carbonate dissolution.

We then kept the effective stress constant at 30 MPa for a period of 21 days (namely Stage 4) and measured permeability every 4–5 days, followed by an unloading/reloading cycle (namely Stage 5). There is a slight reduction in argon permeability by 21% over a period of three weeks. Because argon is a non-reactive fluid, the gradual decrease in
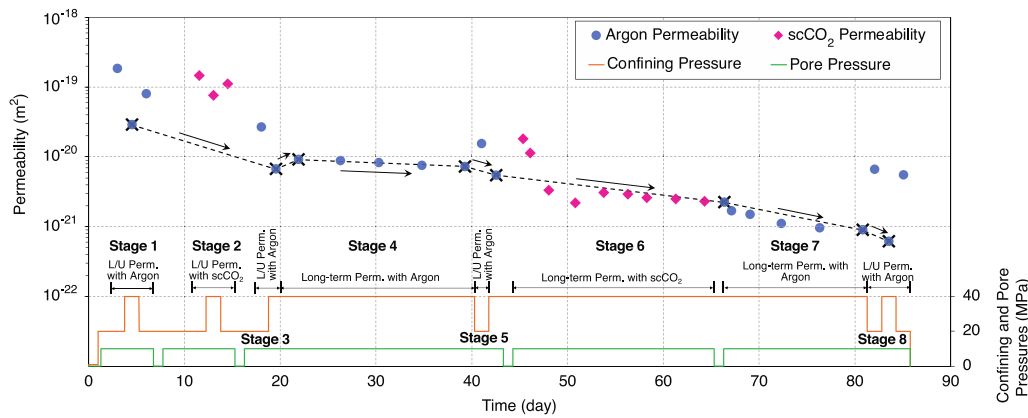
Fig. 2. Permeability evolution of sample 6-1H.

argon permeability could be attributed to (mechanical) viscoplastic deformation under constant effective stress. Many researchers have studied the mechanical deformation, as a result of viscoplastic creep in shale rocks (e.g., Sone and Zoback, 2013b; Kamali-Asl et al., 2018; Rassouli and Zoback, 2018); however, as stated earlier, the effects of viscoplastic deformation on permeability of shale rocks have not been studied. The pressure dependencies of argon permeability before (i.e., Stage 3) and after (i.e., Stage 5) three-week-long creep-type stage of the experiment are 75% and 65%, respectively. The reduced pressure dependency of argon permeability, after maintaining constant effective stress for three weeks, is another indication that mechanical creep is happening in the sample leading to pore compaction, and in turn, reduced pressure dependency of the permeability. Another possible explanation for the reduced pressure dependency might be the precipitation of already-dissolved minerals, so that increasing the effective stress does not alter the accessibility of clogged pore throats.

It is worth noting that unloading/reloading cycle in Stage 5 resulted in 25% reduction in permeability, when the permeability values at $\sigma' = 30$ MPa before and after Stage 4 (i.e., before and after long-term permeability test with argon) are compared. This observation could be associated with the viscoplastic nature of mechanical creep deformation in which an unloading/reloading cycle leads to enhanced pore compaction.

In Stage 6, we re-introduced scCO$_2$ into the sample and let it interact for three weeks under constant effective stress of 30 MPa. We measured CO$_2$ permeability every 1–3 days. Unlike argon (i.e., Stage 4), the CO$_2$ permeability values show a greater decline over time from 18.1 nD to 2.31 nD. This is caused by the reactive nature of CO$_2$, as opposed to unreactive argon, particularly in its supercritical state. We believe that geochemical processes (such as cycles of dissolution/precipitation and adsorption) in addition to mechanical creep are among the processes that cause this behavior. We observe a steeper decrease of permeability compared to argon as indicated by the slope of the dashed line in Fig. 2.

Argon was again introduced into the sample, in Stage 7, and the permeability was measured every 3–5 days over a period of 17 days, under constant $\sigma' = 30$ MPa. The argon permeability gradually decreased from 2.2 nD to 0.9 nD, showing a reduction of ~60%. The slope of the dashed line for the 17-day argon stage (namely Stage 7), after three-week interaction with scCO$_2$, is greater than that of three-week argon stage (namely Stage 4), before three-week interaction with scCO$_2$. The enhanced time-dependent permeability reduction is related to the effects of scCO$_2$ on chemo-mechanical creep behavior of shale, particularly in samples with a meaningful degree of carbonate dissolution. Lastly, an unloading/reloading/unloading cycle is performed and argon permeabilities are measured in Stage 8. This last cycle shows a pressure dependency of 89% when transitioning from an effective stress of 30 to 10 MPa, while it was 65% in Stage 5, right before three-week interaction with scCO$_2$. This is another indication that

interaction with scCO$_2$ leads to enhanced chemo-mechanical creep in this sample. In addition, the unloading/reloading cycle in Stage 8 led to reduction in permeability by ~16%, which is lower than that of Stage 5.

Overall, we believe that this sample experiences carbonate dissolution in the earlier times of the experiment, leading to permeability increase in Stage 2. As we conduct long-term permeability experiments, we notice a gradual decrease in permeability by about two orders of magnitude. Our interpretation of data is that over longer time periods the increase of permeability due to carbonate dissolution is overweighted by the decrease of permeability by (i) matrix weakening caused by dissolution of carbonate minerals, and (ii) potential precipitation of dissolved (carbonate) minerals.

Fig. 3 presents the BSE/EDS images of three regions in sample 6-1H at magnifications of 3500X, 6500X, and 8000X. We observe that there are multiple regions with carbonate dissolution and multiple regions with precipitation of dissolved minerals. By inspecting the EDS maps of carbon and calcium in Fig. 3(b) and (c) (Mag: 3500X), carbonate dissolution is spotted in region R1-1. Regions R2-1 and R3-1, however, show minor surface etching/alteration.

We also observe regions with carbonate dissolution and mineral precipitation in Fig. 3(d) – 3(f) (mag: 6500X). Carbonate dissolution is seen in region R1-2, as concluded by comparing the EDS maps of carbon and calcium. Precipitation of minerals on the surface of the sample is seen in regions R2-2 and R3-2. The microstructure of the carbonate grain (here dolomite) seems to be unaltered in regions R4-2 and R5-2, consistent with the lesser reactivity of dolomite as compared to calcite. As observed in Fig. 3(g) – 3(i) (mag: 8000X), there are two carbonate grains. In Fig. 3(g) (like regions in Fig. 3(a) and (d)), we distinguish between some sub-regions in each grain with carbonate dissolution (i.e., regions R3-3 and R4-3), while some sub-regions are not affected (regions R1-3 and R2-3). The imaging observations are consistent with our interpretation that carbonate dissolution resulted in an increase in permeability, followed by decrease of permeability over longer time periods by dissolution-induced matrix weakening and potential precipitation of dissolved minerals.

3.2. Sample 6-3H

Fig. 4 presents the evolution of permeability for sample 6-3H. Tests lasted for about 6 months. Initially, we measured argon permeability at $\sigma' = [10,30]$ MPa in Stage 1, followed by maintaining the constant effective stress at 30 MPa for 25 days. We measured argon permeability every 1–4 days during this stage. We observe a nearly logarithmic increase in argon permeability from 0.354 to 0.518 nD. This increase is associated with the net effects of mechanical loading/relaxation over a period of more than 3 weeks, as argon is a non-reactive fluid.

We then conducted a Klinkenberg-type test (i.e., Stage 2) in order to estimate the average (accessible) pore throat diameter. According to
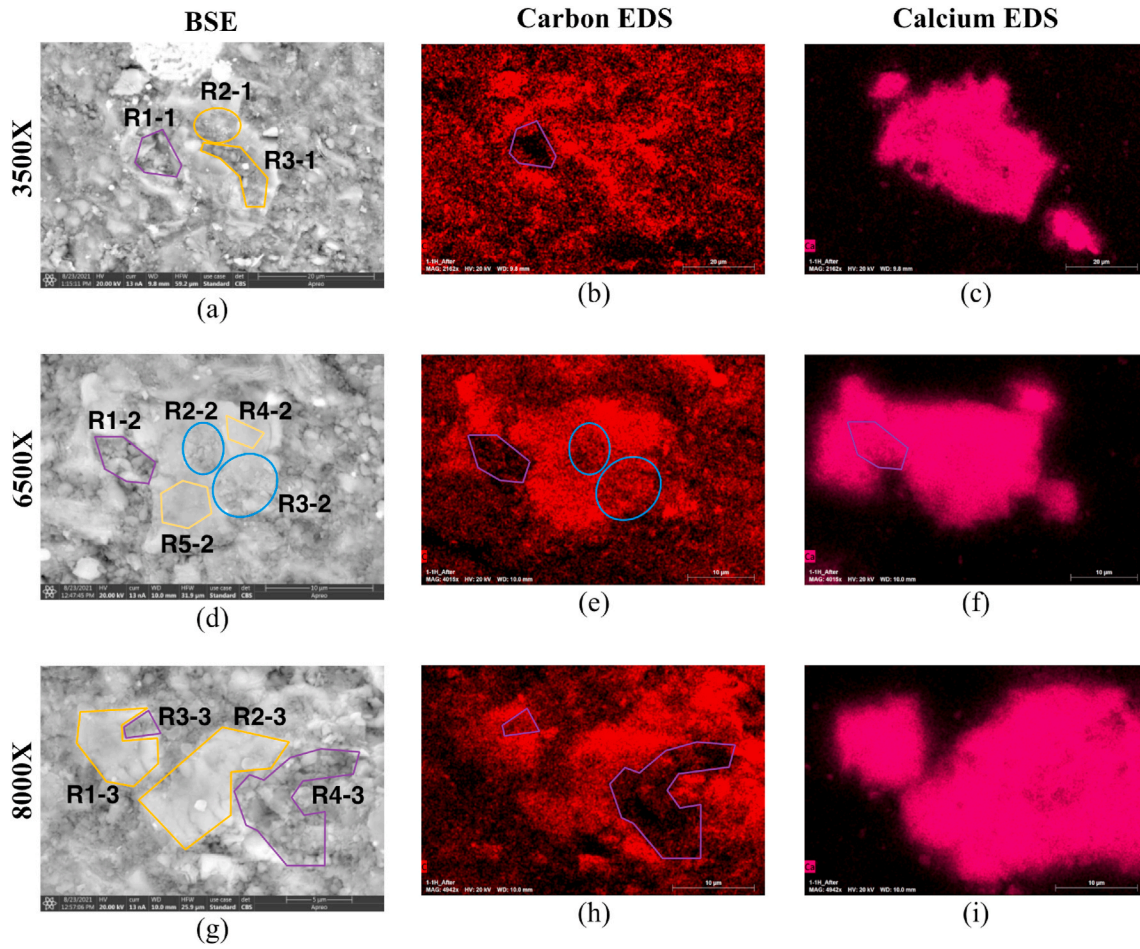
Fig. 3. BSE and EDS (for carbon and calcium) images of three different regions in sample 6-1H at magnifications of (a)–(c) 3500X, (d)–(f) 6500X, (g)–(i) 8000X. Left column: BSE images; middle column: carbon EDS map in red color; right column: calcium EDS map in magenta color.
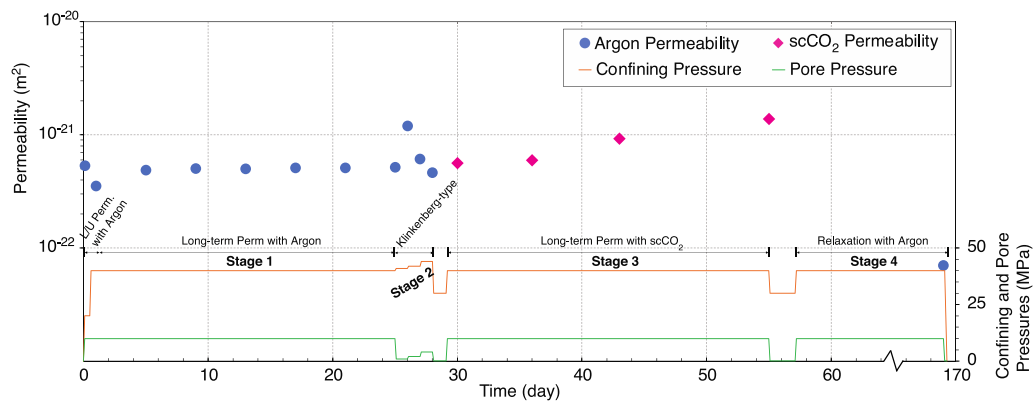

Fig. 4. Permeability evolution for sample 6-3H.

Klinkenberg, to account for slip effects, we have

$$k_{gas} = k_{\infty} \left(1 + \frac{b_{slip}}{p} \right) \quad (3)$$

where k_{gas} is the apparent permeability measured by gas (m²), k_{∞} is the permeability at infinite pressure (m²), b_{slip} is the Klinkenberg slip parameter (m), and p is the mean pore pressure across the sample (Pa).

Assuming pores as spheres, we have

$$r = \frac{4}{b_{slip}} \times \frac{K_B T}{\sqrt{2}\pi d^2} \quad (4)$$

in which r is the average pore throat radius (m), d is the molecular diameter of the flowing gas (m), T is the temperature (K), and K_B is the Boltzmann constant (1.381×10^{-23} m² kg.s^{-2}. K^{-1}).

Fig. 5 shows the permeability data from the Klinkenberg-type portion of the main experiment (i.e., Stage 2), where the permeability data is plotted against 1/P. We estimate the Klinkenberg slip parameter $b_{slip} = 5.92$ MPa and average pore throat radius r = 5.7 nm.
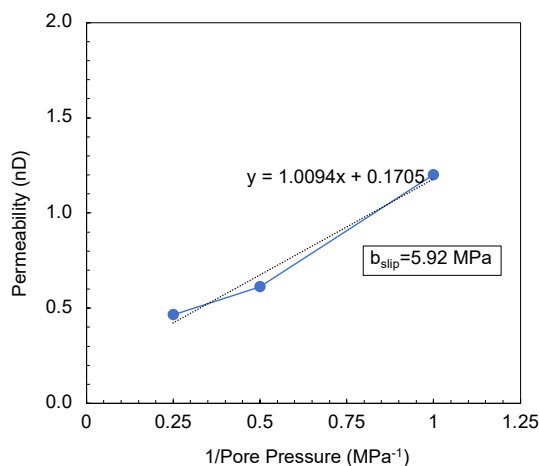
Fig. 5. Klinkenberg plot of permeability vs. $1/P_P$ for sample 6-3H.

Stage 3 of the experiment was conducted using $scCO_2$ as the pore fluid. We initially let the sample interact with $scCO_2$ for two days, then measured the CO_2 permeability. We maintained the constant effective stress at 30 MPa for a period of 26 days, and measured CO_2 permeability after 2, 7, 14, and 26 days. As obvious in Fig. 4, the CO_2 permeability exponentially increases from 0.564 to 1.39 nD, exhibiting ~150% increase in its permeability. Lastly, in Stage 4, we let the sample relax with argon (as the pore fluid) during the Covid-19 closure for ~100 days. Subsequently, we measured the argon permeability as < 0.1 nD. The exponential increase in permeability, given the large amount of carbonates in the sample, could be associated with carbonate dissolution. Similar to sample 6-1H, we observe a significant decrease in permeability over longer time periods. This, again, could be associated with dissolution-induced matrix weakening or precipitation of already-dissolved minerals. Despite the significantly larger carbonate content of this sample (67%) and smaller TOC (1%) as compared to sample 6-1H (21% carbonate and 3% TOC), we cannot attribute the different permeability response of the two samples to only different degrees of carbonate dissolution, although it plays a very important role, because the testing procedure for the two samples are slightly different.

3.3. Sample 6-4H

We conducted a 4-month experiment on sample 6-4H that consisted of three stages, as shown in Fig. 6. In Stage 1, we performed argon permeability tests at $\sigma' = [10,30]$ MPa, exhibiting 15% reduction in permeability when increasing the effective stress from 10 to 30 MPa. We

then kept the effective stress constant for a period of 24 days, and measured permeability every 3–6 days. We observed that the permeability decreased from 230 to 124 nD, in the first 6 days of Stage 1. The argon permeability then gradually recovered to 224 nD over a period of 18 days. The pressure dependency of the sample at the end of the Stage 1, increased to 18%, after 24-day relaxation with argon.

After introducing CO_2 into the sample, we performed Stage 2 of the experiment, in which the sample interacted with $scCO_2$ for ~9 weeks. We measured CO_2 permeability every 1–4 days. The sudden drop of permeability, from the last argon measurement (242.6 nD) to the first CO_2 measurement (65.1 nD), is likely to be caused by adsorption of CO_2 into clays and organic matter (Kamali-Asl et al., 2021). Recall that the TOC of this sample is 6%. As perceived in Fig. 6, cycles of increase/-decrease in CO_2 permeability occur over the 9-week period of interaction/relaxation. We believe that the cycles of increase in permeability are associated with local carbonate dissolution and cracks induced by kerogen-swelling, while the cycles of permeability reduction are associated with precipitation of (i) already-dissolved minerals, and/or (ii) salts somewhere along the flow path. Overall, we observe that the CO_2 permeability increases from 65.1 to 90.5 nD over a period of 9 weeks.

We concluded the test by conducting a 24-day relaxation stage with argon and measuring permeability every 2–4 days, namely Stage 3. Upon removing CO_2 (and re-introducing argon), the sample experiences a sudden increase in its permeability from 90.5 to 154.2 nD, due to recoverability of adsorption phenomenon as we discussed in our previous work (Kamali-Asl et al., 2021). The long-term permeability evolution with argon indicates a nearly logarithmic increase, from 154.2 to 246 nD, over a period of 24 days. Moreover, we observe that pressure sensitivity of argon permeability (transitioning from $\sigma' = 10$–30 MPa) increases to 32%, while it was only 18% before 11-week interaction/relaxation with $scCO_2$. Both the gradual increase of argon permeability over time and the enhanced pressure sensitivity of permeability reveal that (i) new flow conduits were created, and (ii) carbonate may contribute to permeability evolution of sample 6-4H.

Figs. 7–10 provide the BSE/EDS images of multiple regions in sample 6-4H. We observe that the most affected elements are organic matter and carbonate minerals. Fig. 7 shows that there are some regions (namely, R1 and R2), within the organic matter, where salt precipitation and pyrite oxidization coincide with the micro-cracks. We believe that this is associated with adsorption of CO_2 into organic matter, and subsequently, the creation of swelling-induced cracks within the organic matter, while CO_2 interacts with pore water leading to salt precipitation and oxidization of pyrite in the presence of H^+. The fact that larger cracks (i.e., those in the vicinity of region R1) are present in regions where more substantial pyrite oxidation and salt precipitation occurs (i.e., region R1) is another indication that swelling-induced cracks are created within the organic matter. While salt precipitation leads to
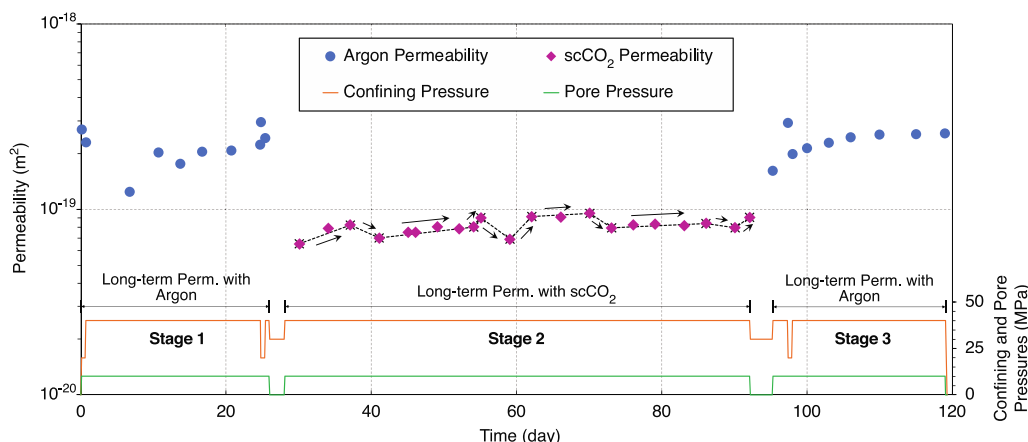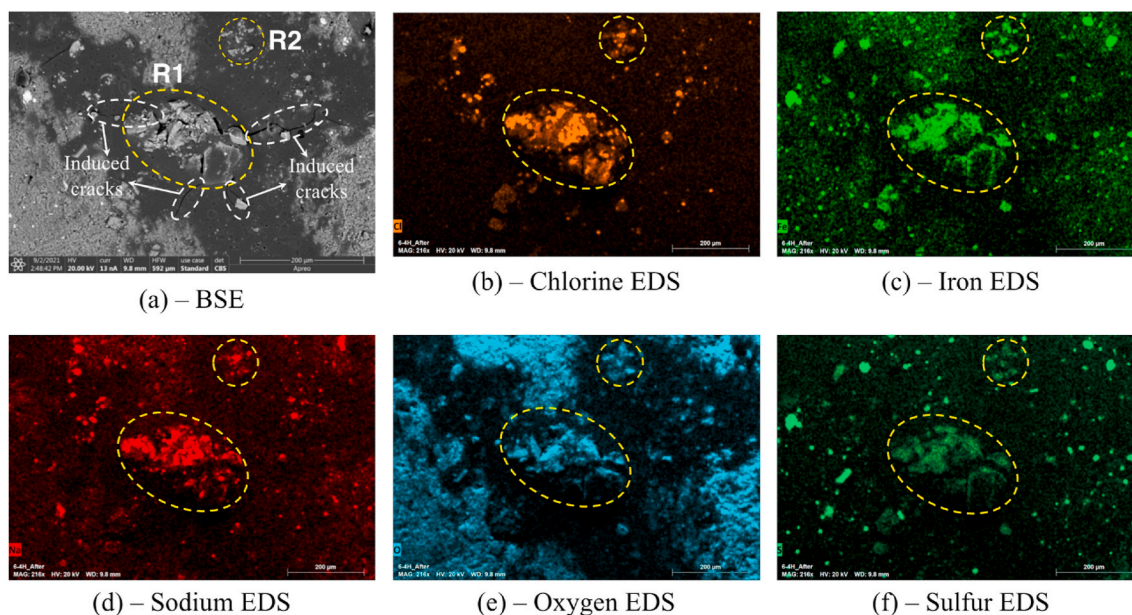

Fig. 6. Permeability evolution for sample 6-4H.

(a) – BSE

(b) – Chlorine EDS

(c) – Iron EDS

(d) – Sodium EDS

(e) – Oxygen EDS

(f) – Sulfur EDS

Fig. 7. BSE and EDS images for region I, at a magnification of 350X, in sample 6-4H. Fig. 7(a) represents BSE results, while Fig. 7(b)–(f) represent EDS maps for chlorine, iron, sodium, oxygen, and sulfur, respectively.

(a) – BSE

(b) – Carbon EDS

(c) – Chlorine EDS

(d) – Iron EDS

(e) – Sodium EDS

(f) – Sulfur EDS
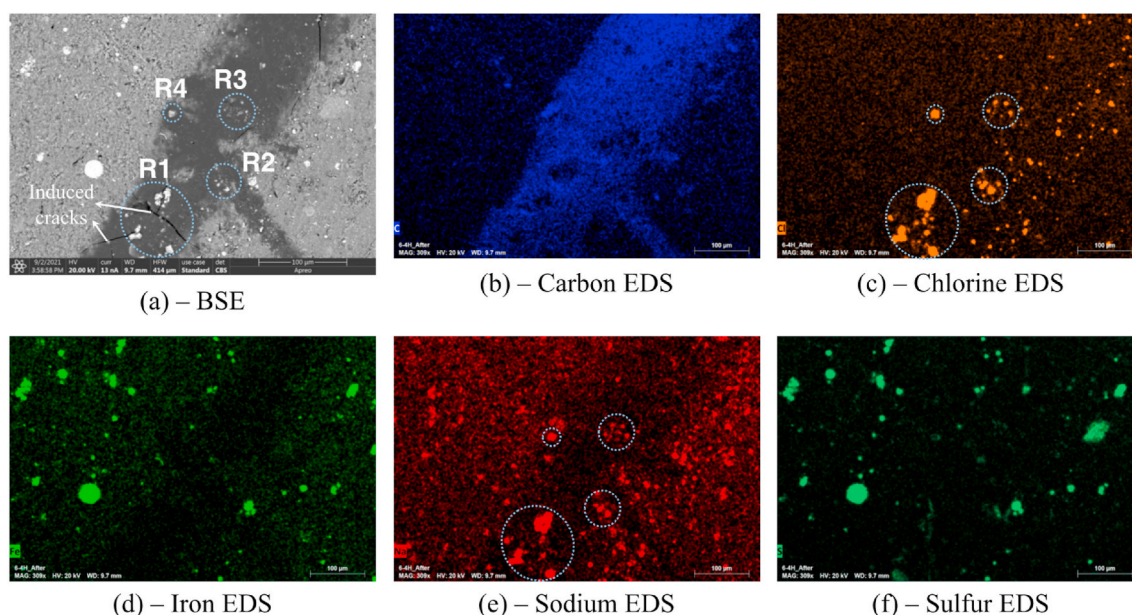
Fig. 8. BSE and EDS images for region II, at a magnification of 500X, in sample 6-4H. Fig. 8(a) represents BSE results, while Fig. 8(b)–(f) represent EDS maps for carbon, chlorine, iron, sodium, and sulfur, respectively.

permanent reduction in permeability, the induced cracks might increase the permeability by creating new flow channels or decrease it by increasing the compliance of the rock matrix.

Fig. 8 provides the BSE/EDS images of region II on sample 6-4H, where swelling-induced cracks coexist with salt precipitation. R1 is the most affected region in which the largest induced crack is present, and it is associated with a notable degree of salt precipitation. The white bright crystals of Region R1 in the BSE image (i.e., Fig. 8(a)) are salt crystals. We drew this conclusion by concurrent inspection of chlorine (Fig. 8(c)) and sodium (Fig. 8(e)) EDS maps, alongside the BSE image. Considering the EDS maps of chlorine (Fig. 8(c)) and sodium (Fig. 8(e)) for Regions R2 – R4, along with the associated regions in BSE image, we also observe salt precipitation in Regions R2 – R4, however, to a much

smaller extent. It should be noted that, unlike region I (as shown in Fig. 7), pyrite oxidization does not occur near the cracks. This is simply because there is no pyrite present in the vicinity of the cracks. It is also important to mention that not all the cracks within the organic matter are swelling-induced.

Figs. 9 and 10 show the BSE/EDS images of regions III and IV, respectively. As evident in both figures, there are some salt precipitates that occur within the carbonate grains (R2's for both regions III and IV), while we observe surface etching and carbonate dissolution in the rest of the grains (R1's in both regions).

What we observed in Figs. 7–10, is very complex because there are at least four distinct phenomena that coincide/concur. These are (i) adsorption of CO_2 into organic matter, (ii) creation of swelling-induced
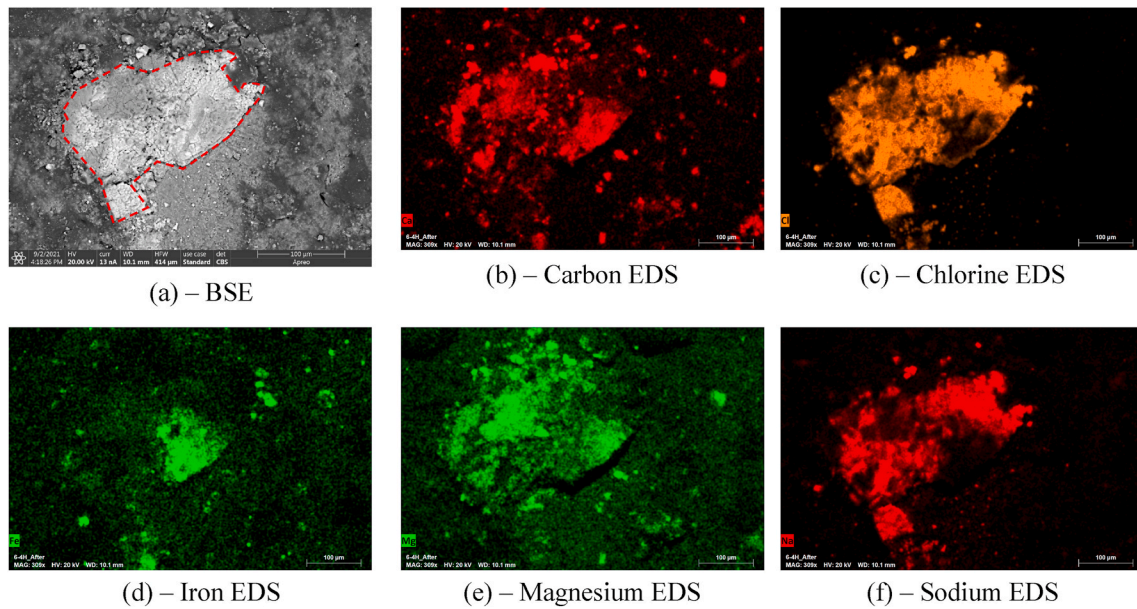
Fig. 9. BSE and EDS images for region III, at a magnification of 500X, in sample 6-4H. Fig. 9(a) represents BSE results, while Fig. 9(b)–(f) represent EDS maps for calcium, chlorine, iron, magnesium, and sodium, respectively.
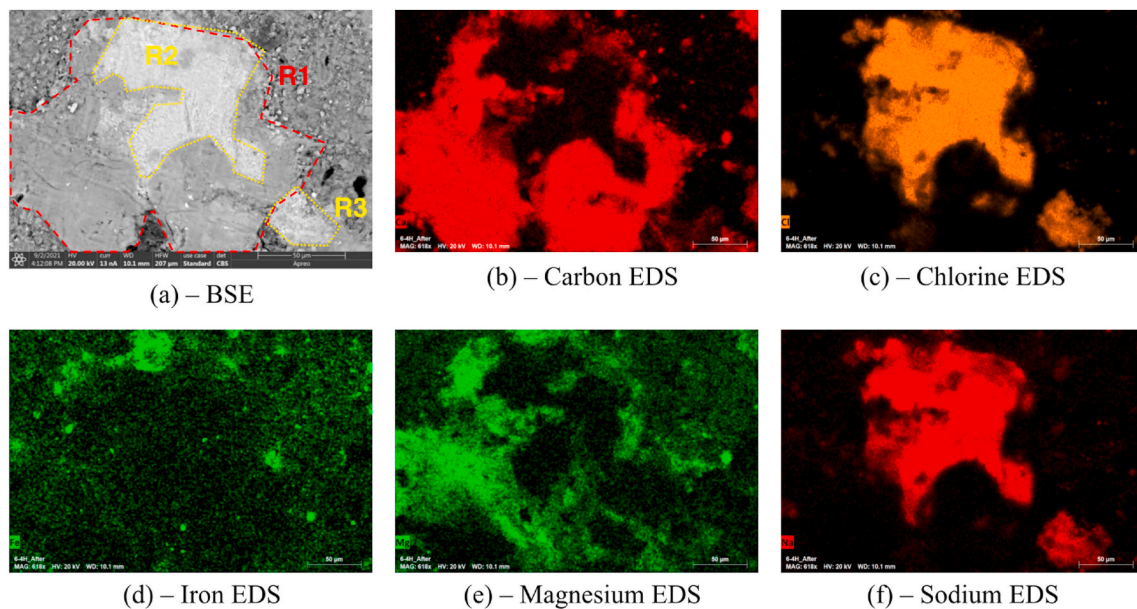

Fig. 10. BSE and EDS images images for region IV, at a magnification of 1000X, in sample 6-4H. Fig. 10(a) represents BSE results, while Fig. 10(b)–(f) represent EDS maps for calcium, chlorine, iron, magnesium, and sodium, respectively.

cracks within organic matter, (iii) salt precipitation within carbonate minerals and organic matter, and (iv) carbonate dissolution. By combining the permeability data (i.e., Fig. 6) and the BSE/EDS images, we believe that the effects of salt precipitation on reducing the permeability is overshadowed by the effects of induced cracks on increasing the permeability.

3.4. Sample 1-1H

Fig. 11 shows the evolution of permeability for sample 1-1H, over a period of 14 weeks. Unfortunately, in this experiment, we were not able to make any reliable CO_2 measurements. This was due to technical issues with insulation limiting maintenance of constant temperature, which is a key parameter in being able to measure CO_2 permeability, because of

substantial temperature sensitivity of CO_2 properties (namely, compressibility and viscosity).

In Stage 1, we first measured argon permeability at $\sigma' = 10$ and 30 MPa in order to obtain the pressure sensitivity of permeability before any long-term test. Transitioning from an effective stress of 10–30 MPa, the argon permeability decreased from 8.5 to 6.9 nD. Maintaining the effective stress at 30 MPa for a period of 24 days resulted in an exponential decay of permeability, as indicated by the dashed line in Fig. 11, from 6.9 to 6.1 nD. The permeability decay signifies the closure (or reduction in diameter) of pore throats due to mechanical creep. The pressure sensitivity decreased from 19% (at the beginning of Stage 1; before long-term relaxation with argon) to 14% (at the end of Stage 1; after long-term relaxation with argon). The reduction in pressure sensitivity is another indication that the pore throats are narrowed or
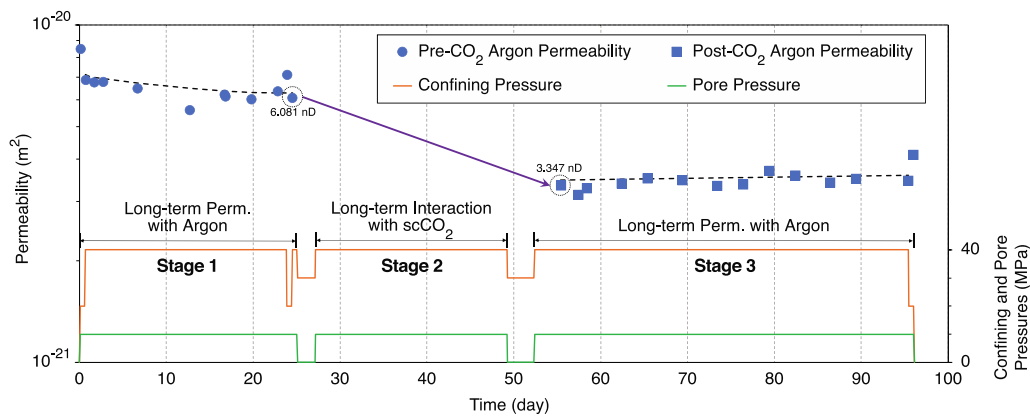
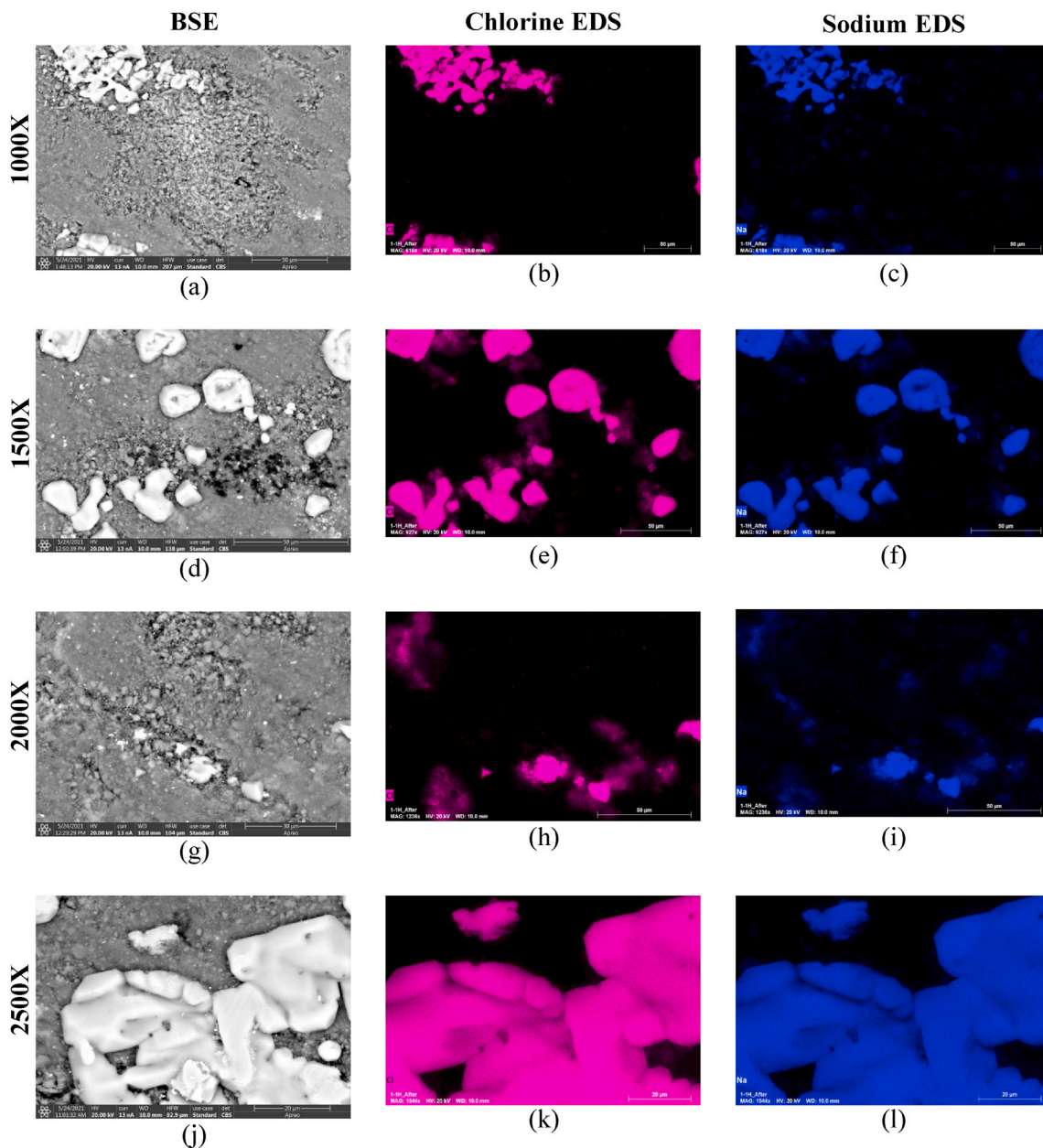**Fig. 11.** Permeability evolution for sample 1-1H.

Fig. 12. BSE and EDS (for chlorine and sodium) images of four different regions in sample 1-1H at magnifications of (a)–(c) 1000X, (d)–(f) 1500X, (g)–(i) 2000X, and (j)–(l) 2500X. Left column: BSE images; middle column: chlorine EDS maps in magenta color; right column: sodium EDS maps in blue color.

closed, and therefore, the rock matrix (in the vicinity of flow path) becomes stiffer.

As acknowledged earlier, we were not able to make any permeability measurements during the 25 days of interaction/relaxation with scCO$_2$ (i.e., Stage 2). We can certainly state, however, that the rock matrix has interacted with scCO$_2$. Therefore, we expect that the argon permeability changes after long-term interaction with supercritical CO$_2$. In Stage 3, we reintroduced argon into the sample and let it relax with argon under constant effective stress of 30 MPa for a period of 44 days, and measured permeability every 1–5 days. When the last permeability value in Stage 1 is compared to the first permeability value in Stage 3, we observe that the argon permeability decreases by 45% from a value of 6.08 to 3.35 nD. The time-dependent argon permeability exhibits a relatively constant value that only increases 3% (from 3.35 to 3.45 nD) over the period of 44 days. At the end of Stage 3, in order to evaluate the pressure sensitivity, we measured permeability at an effective stress of 10 MPa. We observe that permeability increases from 3.45 to 4.12 nD, exhibiting a 16% increase when transitioning from $\sigma' = 30$ to 10 MPa. This is a slight increase in pressure sensitivity compared to the pressure sensitivity at the end of Stage 1 (16% vs. 14%).

In order to better interpret the results of this experiment, we obtained BSE and EDS (for chlorine and sodium elements) images for different regions of the sample surface. Fig. 12 shows four different regions at magnifications of 1000X, 1500X, 2000X, and 2500X. We observe salt (halite) precipitation in these regions as indicated by the mutual presence of chlorine and sodium, while the extent of dissolution/precipitation is minor. Based on the available data and the images, we believe that the 25-day interaction with scCO$_2$ was mainly associated with salt precipitation. While carbonate dissolution and adsorption of CO$_2$ into clays and kerogen played a minor role. The latter would dissipate as we re-introduce argon, however, carbonate dissolution and salt precipitation are not recoverable after re-introducing argon. Therefore, the decrease in permeability in Stage 3 compared to Stage 1 is consistent with salt precipitates blocking the fluid flow path but we cannot say so unequivocally.

4. Discussion

In this section, an in-depth discussion is provided about the permeability evolution during pre-reaction argon, CO$_2$, and post-reaction argon stages. Focus is placed on permeability because it is a primary determiner of field-scale performance. Production decline in shale formations is, in part, caused by permeability decay and the continued efficiency of shaly seals in geological storage of CO$_2$ is primarily dependent on their permeability. Table 2 presents a summary of the duration and differences between the experimental procedure for each sample.

We then examine the absolute change in permeability without considering the permeability evolution within each stage. Fig. 13 presents the first and last permeability measurements during each stage against the carbonate content. The most obvious observation is the inverse correlation between permeability and carbonate content, as also observed by other researchers (Aljamaan et al., 2017; Kamali-Asl et al., 2021). The permeability during the CO$_2$ injection stage experiences larger changes compared to pre-reaction argon stage. This is attributed to the role of geochemical interactions such as dissolution, precipitation, and adsorption. Most importantly, although permeability significantly evolves during interaction with CO$_2$, we observe that the initial permeability predominates over permeability evolution. Sections 4.1–4.3 provide detailed discussion during pre-reaction, CO$_2$, and post-reaction tests.

4.1. Pre-reaction long-term argon permeability (before long-term interaction with scCO$_2$)

The time-dependent permeability evolution of shale rocks, both

Table 2
Summary of the experiments.

Sample ID	Stage	Duration	Description
1-1H	Pre-CO$_2$ (using argon)	24 days	Pressure dependency of permeability was investigated before and after long-term permeability evolution.
	scCO$_2$	25 days	Due to fluctuations in temperature, an exponential curve of downstream pore pressure evolution, and hence permeability, could not be obtained.
	Post-CO$_2$ (using argon)	44 days	Pressure dependency of permeability was considered only at the end of this stage. Duration was prolonged to make sure that the permeability evolution is fully captured.
6-1H	Pre-CO$_2$ (using argon)	21 days	Two cycles of short-term argon and scCO$_2$ permeability tests were performed. We investigated pressure dependency of permeability before and after long-term permeability test.
	scCO$_2$	24 days	We did not investigate pressure dependency of permeability before and after the long-term test to prevent any loading-induced permeability changes.
	Post-CO$_2$ (using argon)	17 days	Two cycles of permeability pressure dependency tests were conducted after completion of long-term post-CO$_2$ permeability test.
6-3H	Pre-CO$_2$ (using argon)	25 days	Pressure dependency cycle was performed before long-term test. A Klinkenberg-type experiment was afterwards conducted to verify that pore throats are extremely narrow.
	scCO$_2$	26 days	No pressure dependency cycle was performed to avoid any loading-induced (mechanical) permeability changes.
	Post-CO$_2$ (using argon)	100 days	The sample was relaxed for an extended period, followed by one single permeability measurement without any loading/unloading.
6-4H	Pre-CO$_2$ (using argon)	24 days	Pressure dependency of permeability was investigated before and after the long-term test.
	scCO$_2$	61 days	No pressure dependency cycle was performed to avoid any loading-induced (mechanical) permeability changes, like other samples.
	Post-CO$_2$ (using argon)	24 days	Pressure dependency cycle was performed at the beginning of long-term permeability test.

before and after long-term interaction with scCO$_2$, strongly depends on their mineral composition, TOC, and micro-structure. Fig. 14 contains the permeability evolution with argon, before long-term interaction with scCO$_2$, under constant effective stress of 30 MPa. We roughly categorize the permeability evolution of the samples into the following three cases:

I) *Moderate permeability decay* in the samples with moderate amounts of carbonates and clays/TOC (namely, samples 1-1H and 6-1H). It is known that shales exhibit substantial viscoplastic deformation (mechanical creep), under constant stress conditions, resulting in closure of pores and cracks, that in turn, leads to loss of porosity. While there is not necessarily a universal relationship between porosity and permeability, we expect that a reduction in porosity (due to mechanical creep) is associated with a reduction in permeability. Therefore, we believe that mechanical creep is responsible for the permeability decay in these two samples. The *reduction in pressure dependency* of permeability after the (pre-reaction) long-term argon test, for both samples, is another indication that viscoplastic deformation is present in
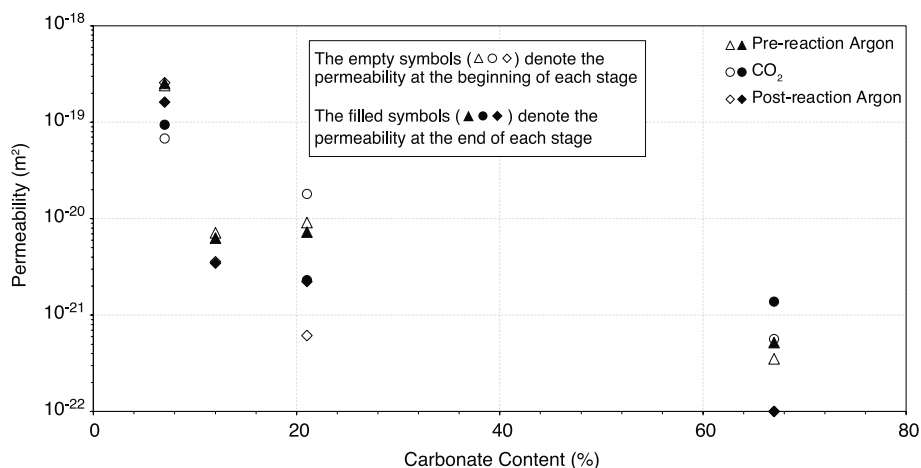
Fig. 13. First and last permeability measurements during pre-reaction argon, CO₂, and post-reaction argon tests against the carbonate content of the samples. Overwhelmingly, initial permeability is a major factor in the outcome of each stage of injection.
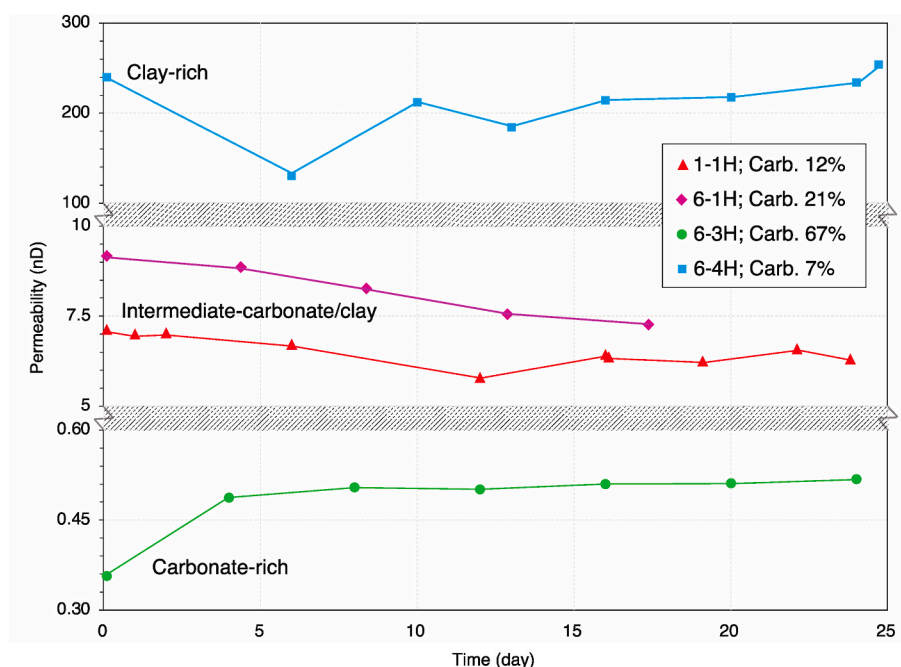

Fig. 14. Long-term evolution of pre-reaction argon permeabilities (before long-term interaction with scCO₂). Carbonate content of each sample given in the legend.

these samples, causing enhanced pore compaction and reducing its compliance.

II) *Slight permeability increase* in the carbonate-rich and small TOC sample (6-3H), that occurs primarily in the first few days of the test, followed by practically constant permeability over the next three weeks.

III) *Relatively constant permeability* in the clay-rich/kerogen sample. It should be, however, noted that the permeability decreases by half in the first week of the test, followed by almost full recovery in the next three weeks.

The (initial) permeability values of samples 6-1H, 6-3H, and 6-4H differ by ~3 orders of magnitude, while their retrieval depths are within 85 ft of each other. The remarkable permeability variation and the substantial difference in mineral composition of the samples, within such a short depth interval, highlights the significance of the sample dependency in transport behavior of these samples.

4.2. Long-term permeability evolution with scCO₂

Fig. 15 shows the permeability evolution with scCO₂ for samples 6-1H, 6-3H, and 6-4H. As explained earlier, we could not measure the CO₂ permeability values for sample 1-1H due to experimental limitations. We observe completely distinct phenomena among the samples. *Enhanced permeability decay rate* compared to pre-reaction argon permeability case (for sample 6-1H with moderate amounts of clay/kerogen and carbonate), significant *permeability growth by carbonate dissolution* (for carbonate-rich sample 6-3H), and *cycles of increase and decrease of permeability possibly due to coincidence of salt precipitation and swelling-induced cracks* with a net slight increase (for clay-rich/kerogen sample 6-4H). The sample dependency of permeability response, in this case due to long-term interaction with scCO₂, is discernible by comparing the permeability evolution for different samples. As stated earlier, these three samples are only 85 ft apart, but we identify different behavior in their long-term scCO₂ permeability response.
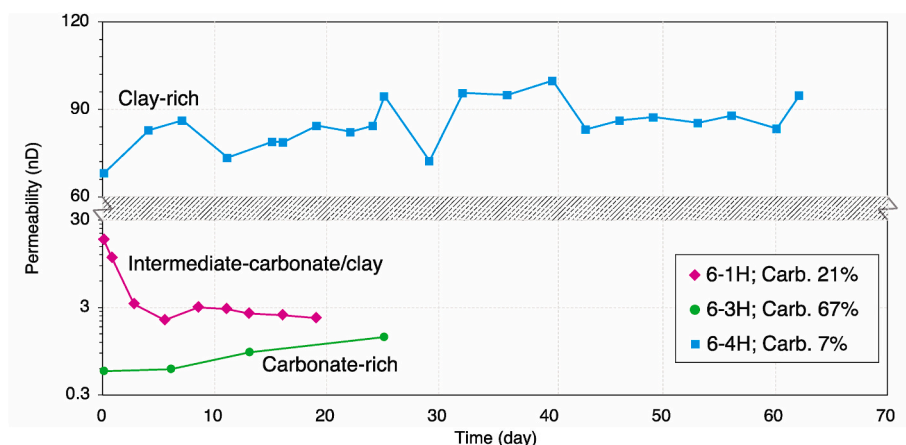
Fig. 15. Evolution of the long-term CO_2 permeabilities. Please note that we could not measure the $scCO_2$ permeability for sample 1-1H due to experimental limitations. Carbonate content of each sample given in the legend.

4.3. Post-reaction long-term argon permeability (after long-term interaction with scCO₂)

The argon permeability evolution of post-reacted samples (after long-term interaction with $scCO_2$) is provided in Fig. 16. We observe the following by exploring the post-reaction argon permeability data and comparing it with the permeability data during (i) the pre-reaction stage with argon, and (ii) the interaction stage with $scCO_2$:

I) *Salt precipitation* most likely led to a sudden decrease in argon permeability after long-term interaction with $scCO_2$ (in sample 1-1H). Although the long-term evolution of argon permeability, after interaction with $scCO_2$, shows relatively constant values. Considering that sample 1-1H had exhibited (i) permeability decay during its pre-reaction long-term argon test, and (ii) sudden drop in its permeability after the long-term $scCO_2$ test, we anticipated relatively constant post-reaction argon permeability. The roughly unchanged pressure dependency of permeability at the end of the post-reaction argon test compared to the end of the pre-reaction argon test shows that the rock matrix has not experienced matrix weakening, but rather pore clogging due to salt precipitation.

II) *Dissolution-induced matrix weakening* enhanced the decay of long-term argon permeability, when post-reaction data is compared to pre-reaction, for samples with moderate amounts of carbonates (i.e., sample 6-1H). Matrix weakening is also evident when the

pressure dependency of pre- and post-reaction permeability data are compared. Both greater permeability decay and greater pressure dependency of permeability indicate that the rock matrix is weakened by dissolution of (stiff) carbonate minerals.

III) The *permeability increased post-reaction* during the post-reaction argon test in sample 6-4H. We believe removing CO_2 from the sample halted any further salt precipitation, and in turn, any reduction in permeability; however, gradual opening of swelling-induced cracks (within the organic matter) led to a logarithmic increase in permeability. The larger pressure dependency at the beginning of long-term post-reaction argon test, compared to the end of the long-term pre-reaction argon test, is another indication that the contribution of induced cracks in fluid flow has increased during the post-reaction argon test.

IV) Significant decrease in post-reaction argon permeability of the large-carbonate-content sample (i.e., 6-3H) after a prolonged period of relaxation with argon, despite substantial increases during the long-term CO_2 test. We postulate that this behavior occurred due to significant carbonate dissolution leading to weakening of the rock matrix. Please note that the substantially small permeabilities during the post-reaction argon test prevented us from measuring the long-term evolution of permeability, and hence, we have only reported an initial value for the post-reaction argon test.
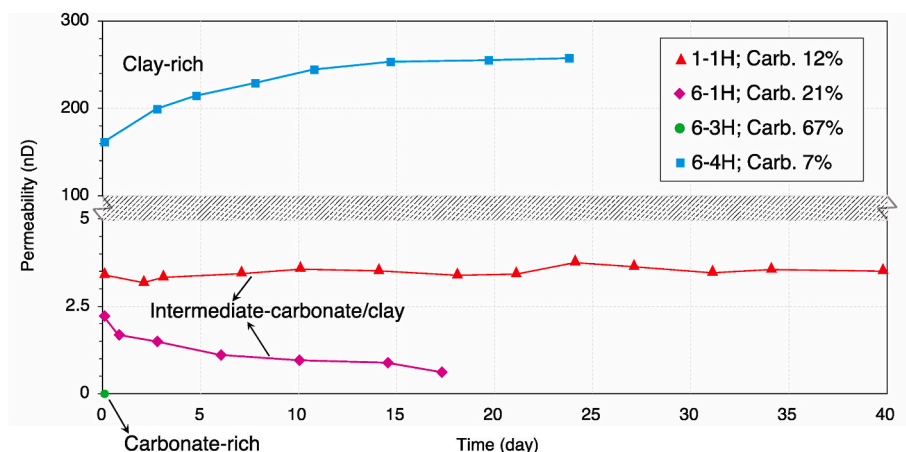

Fig. 16. Long-term evolution of post-reaction argon permeabilities (after long-term interaction with $scCO_2$). Please note that sample 6-3H exhibited very low permeabilities so that it was impractical to measure its evolution. Carbonate content of each sample given in the legend.

5. Conclusions

CO$_2$-fracturing of shale reservoirs is one of the potentially economic solutions to increase CO$_2$ utilization. However, its commercial scale implementation is yet to be addressed. One of the concerns with CO$_2$-fracturing is the long-term interaction between shale rocks and scCO$_2$, under constant stress conditions. In particular, the time-dependent evolution of permeability is important, as it is directly associated with production. In this work, we designed a suite of experiments to investigate the time-dependent permeability evolution of shale reservoirs, under constant stress conditions, before and after long-term interaction with scCO$_2$. We used disk-shaped 1-inch diameter samples with lengths of 0.2–0.3 inches from the Wolfcamp formation to measure their permeability with argon (before and after interaction with CO$_2$) and scCO$_2$, as the pore fluids. Each stage of testing lasted for one to three months under constant effective stress. This unique stress path enabled us to make direct comparisons between the long-term permeability evolution of shale rocks under argon and scCO$_2$ cycles. We found that the response is highly sample-dependent, and the role of mineralogy and micro-structure of the shale fabric is pronounced.

While the samples with moderate amounts of both carbonates and clay/kerogen showed a slight decay in their pre-reaction long-term argon permeabilities, the low- and high-clay samples exhibited relatively constant long-term argon permeability. In intermediate-to-high clay/kerogen samples, interaction with scCO$_2$ led to salt precipitation with (out) co-occurrence of swelling-induced cracks that resulted in cycles of increase/decrease of permeability during long-term CO$_2$ tests. The post-reaction argon permeabilities, for intermediate-to-high clay/kerogen samples, exhibited: (i) significant drop in argon permeability as compared to pre-reaction data, followed by relatively constant long-term permeability values, and (ii) almost full permeability recovery in the sample in which salt precipitation coincides with swelling-induced cracks, caused by enhanced contribution of induced cracks post-reaction. In the intermediate-to-high carbonate samples, on the other hand, we observed matrix weakening caused by dissolution of carbonates. In the intermediate-carbonate sample, the evolution of both long-term CO$_2$ permeability and post-reaction long-term argon permeability showed enhanced permeability decay, owing to weakening of the matrix. The high-carbonate-content sample, however, exhibited a significant increase of permeability during long-term CO$_2$ injection followed by a significant reduction in its post-reaction argon permeability after relaxation for 100 days. Our results indicated that while the long-term exposure to scCO$_2$ affected the permeability of the samples, the three-order-of-magnitude difference in the samples' initial permeabilities overshadowed the role of long-term evolution of permeability.

Author statement

Arash Kamali-Asl: Experiments, Investigation, Writing – original draft, Revision. **Anthony R. Kovscek**: Supervision, Writing – review & editing, Funding acquisition. **Mark D. Zoback**: Conceptualization, Supervision, Writing – review & editing, Funding acquisition.

Declaration of competing interest

The authors declare that they have no known competing financial interests or personal relationships that could have appeared to influence the work reported in this paper.

Acknowledgments

References

Al Ismail, M., Reece, J.S., Hol, S., Zoback, M., 2014. The Effect of CO2 Adsorption on Permeability Anisotropy in the Eagle Ford Shale. Unconventional Resources Technology Conference (URTEC).

Al Shafloot, T., Kim, T.W., Kovscek, A.R., 2021. Investigating fracture propagation characteristics in shale using sc-CO2 and water with the aid of X-ray Computed Tomography. J. Nat. Gas Sci. Eng. 92, 103736.

Aljamaan, H., Ross, C.M., Kovscek, A.R., 2017. Multiscale imaging of gas storage in shales. SPE J. 22, 1760–1777, 06.

Ao, X., Lu, Y., Tang, J., Chen, Y., Li, H., 2017. Investigation on the physics structure and chemical properties of the shale treated by supercritical CO2. J. CO2 Util. 20, 274–281.

Atkinson, B.K., 1979. A fracture mechanics study of subcritical tensile cracking of quartz in wet environments. Pure Appl. Geophys. 117 (5), 1011–1024.

Brace, W., Walsh, J.B., Frangos, W.T., 1968. Permeability of granite under high pressure. J. Geophys. Res. 73 (6), 2225–2236.

Chhatre, S.S., Sinha, S., Braun, E.M., Esch, W.L., Determan, M.D., Passey, Q.R., et al., 2014, August. Effect of stress, creep, and fluid type on steady state permeability measurements in Tight liquid unconventional reservoirs. In: SPE/AAPG/SEG Unconventional R*esources Technology Conference*.

Ciezobka, J., Courtier, J., Wicker, J., 2018, July. Hydraulic fracturing test site (HFTS)-project overview and summary of results. In: SPE/AAPG/SEG Unconventional Resources Technology Conference. OnePetro.

Elkady, Y., Kovscek, A.R., 2020. Multiscale study of CO2 impact on fluid transport and carbonate dissolution in Utica and Eagle Ford shale. J. Petrol. Sci. Eng. 195, 107867.

Fatah, A., Bennour, Z., Ben Mahmud, H., Gholami, R., Hossain, M., 2020. A Review on the influence of CO2/shale interaction on shale properties: implications of CCS in shales. Energies 13 (12), 3200.

Foroutan, M., Ghazanfari, E., Amirlatifi, A., Perdrial, N., 2021. Variation of pore-network, mechanical and hydrological characteristics of sandstone specimens through CO2-enriched brine injection. Geomechanics for Energy and the Environment 26, 100217.

Gandossi, L., Von Estorff, U., 2013. An overview of hydraulic fracturing and other formation stimulation technologies for shale gas production. Eur. Commisison Jt. Res. Cent. Tech. Reports, 26347.

Hadian, P., Rezaee, R., 2020. The effect of supercritical CO2 on shaly caprocks. Energies 13 (1), 149.

Hakso, A., Zoback, M., 2019. The relation between stimulated shear fractures and production in the Barnett Shale: implications for unconventional oil and gas reservoirs. Geophysics 84 (6), B461–B469.

Heller, R., Zoback, M., 2014. Adsorption of methane and carbon dioxide on gas shale and pure mineral samples. Journal of Unconventional Oil and Gas Resources 8, 14–24.

Heller, R., Vermylen, J., Zoback, M., 2014. Experimental investigation of matrix permeability of gas shales. AAPG (Am. Assoc. Pet. Geol.) Bull. 98 (5), 975–995.

Kamali-Asl, A., Ghazanfari, E., Newell, P., Stevens, M., 2018. Elastic, viscoelastic, and strength properties of Marcellus Shale specimens. J. Petrol. Sci. Eng. 171, 662–679. https://doi.org/10.1016/j.petrol.2018.05.074.

Kamali-Asl, A., Zoback, M.D., Kohli, A.H., 2021. Effects of supercritical CO2 on matrix permeability of unconventional formations. Energies 14 (4), 1101.

Kutchko, B., Sanguinito, S., Natesakhawat, S., Cvetic, P., Culp, J.T., Goodman, A., 2020. Quantifying pore scale and matrix interactions of SCCO2 with the Marcellus shale. Fuel 266, 116928.

Lindner, E.N., 2016. Review of the Effects of CO2 on Very-Fine-Grained Sedimentary Rock/Shale–Part II: Clay Mineral & Shale Response to Hydration. National Energy Technology Laboratory-Energy Data eXchange, NETL. No. 68913329-03d5-45bc-b32a-a7e8e763b10a).

Lindner, E.N., 2017. Review of the Effects of CO2 on Very-Fine-Grained Sedimentary Rock/Shale–Part III: Shale Response to CO2 (No. e4c4b95d-1197-448c-8f0f-89f7d6c886df). National Energy Technology Laboratory-Energy Data eXchange; NETL.

Liu, F., Lu, P., Griffith, C., Hedges, S.W., Soong, Y., Hellevang, H., Zhu, C., 2012. CO2–brine–caprock interaction: reactivity experiments on Eau Claire shale and a review of relevant literature. Int. J. Greenh. Gas Control 7, 153–167.

Lu, J., Nicot, J.P., Mickler, P.J., Ribeiro, L.H., Darvari, R., 2016. Alteration of Bakken reservoir rock during CO2-based fracturing—an autoclave reaction experiment. Journal of Unconventional Oil and Gas Resources 14, 72–85.

Lyu, Q., Long, X., Ranjith, P.G., Tan, J., Kang, Y., Wang, Z., 2018. Experimental investigation on the mechanical properties of a low-clay shale with different adsorption times in sub-/super-critical CO2. Energy 147, 1288–1298.

Meng, M., Ge, H., Shen, Y., Li, L., Tian, T., Chao, J., 2020. The effect of clay-swelling induced cracks on shale permeability during liquid imbibition and diffusion. J. Nat. Gas Sci. Eng. 83, 103514.

Middleton, R.S., Carey, J.W., Currier, R.P., Hyman, J.D., Kang, Q., Karra, S., et al., 2015. Shale gas and non-aqueous fracturing fluids: opportunities and challenges for supercritical CO2. Appl. Energy 147, 500–509.

Nooraiepour, M., Fazeli, H., Miri, R., Hellevang, H., 2018. Effect of CO2 phase states and flow rate on salt precipitation in shale caprocks—a microfluidic study. Environmental science & technology 52 (10), 6050–6060.

Rassouli, F.S., Zoback, M.D., 2018. Comparison of short-term and long-term creep experiments in shales and carbonates from unconventional gas reservoirs. Rock Mech. Rock Eng. 51 (7), 1995–2014.

Sanguinito, S., Goodman, A., Tkach, M., Kutchko, B., Culp, J., Natesakhawat, S., Crandall, D., 2018. Quantifying dry supercritical CO_2-induced changes of the Utica Shale. Fuel 226, 54–64.

Sone, H., Zoback, M.D., 2013. Mechanical properties of shale-gas reservoir rocks—Part 2: ductile creep, brittle strength, and their relation to the elastic modulus. Geophysics 78 (5), D393–D402.

Song, X., Guo, Y., Zhang, J., Sun, N., Shen, G., Chang, X., Xue, Z., 2019. Fracturing with carbon dioxide: from microscopic mechanism to reservoir application. Joule 3 (8), 1913–1926. https://doi.org/10.1016/j.joule.2019.05.004.

Teklu, T.W., Abass, H.H., Hanashmooni, R., Carratu, J.C., Ermila, M., 2017. Experimental investigation of acid imbibition on matrix and fractured carbonate rich shales. J. Nat. Gas Sci. Eng. 45, 706–725.

van Noort, R., Yarushina, V., 2019. Water, CO_2 and argon permeabilities of intact and fractured shale cores under stress. Rock Mech. Rock Eng. 52 (2), 299–319.

Wei, M., Liu, J., Shi, R., Elsworth, D., Liu, Z., 2019. Long-term evolution of coal permeability under effective stresses gap between matrix and fracture during CO 2 injection. Transport Porous Media 130 (3), 969–983.

Wu, W., Zoback, M.D., Kohli, A.H., 2017. The impacts of effective stress and CO_2 sorption on the matrix permeability of shale reservoir rocks. Fuel 203, 179–186.

Zhang, C., Ranjith, P.G., 2018. Experimental study of matrix permeability of gas shale: an application to CO2-based shale fracturing. Energies 11 (4), 702.

Zoback, M.D., Kohli, A.H., 2019. Unconventional Reservoir Geomechanics. Cambridge University Press.

Zou, Y., Li, S., Ma, X., Zhang, S., Li, N., Chen, M., 2018. Effects of CO2–brine–rock interaction on porosity/permeability and mechanical properties during supercritical-CO2 fracturing in shale reservoirs. J. Nat. Gas Sci. Eng. 49, 157–168.